Manuscript submitted to
AIMS' Journals
Volume **X**, Number **0X**, XX **2007**

Website: http://AIMsciences.org

pp. **X–XX**

NONLINEAR THREE-DIMENSIONAL SIMULATION OF SOLID TUMOR GROWTH

Xiangrong Li
Department of Mathematics
University of California at Irvine
Irvine, CA 92697, USA

Vittorio Cristini
Department of Biomedical Engineering and Department of Mathematics
University of California at Irvine
Irvine, CA 92697, USA
Present address:
School of Health Information Sciences
University of Texas Health Science Center
Houston, TX 77030, USA

Qing Nie
Department of Mathematics, Center for Mathematical and Computational Biology
and Department of Biomedical Engineering
University of California at Irvine
Irvine, CA 92697, USA

John S. Lowengrub
Department of Mathematics, Center for Mathematical and Computational Biology
University of California at Irvine
Irvine, CA 92697, USA

Dedicated to Professor Frederic Yui-Ming Wan on the occasion of his 70th birthday

(Communicated by Ka-Kit Tung)

2000 *Mathematics Subject Classification.* Primary: 58F15, 58F17; Secondary: 53C35.

Key words and phrases. Solid tumor growth, 3D adaptive boundary integral method, Nonlinear simulation, Morphological instability.

Corresponding author: lowengrb@math.uci.edu.

Abstract. We present a new, adaptive boundary integral method to simulate solid tumor growth in 3-d. We use a reformulation of a classical model that accounts for cell-proliferation, apoptosis, cell-to-cell and cell-to matrix adhesion. The 3-d method relies on accurate discretizations of singular surface integrals, a spatial rescaling and the use of an adaptive surface mesh. The discretized boundary integral equations are solved iteratively using GMRES and a discretized version of the Dirichlet-Neumann map, formulated in terms of a vector potential, is used to determine the normal velocity of the tumor surface. Explicit time stepping is used to update the tumor surface. We present simulations of the nonlinear evolution of growing tumors. At early times, good agreement is obtained between the results of a linear stability analysis and nonlinear simulations. At later times, linear theory is found to overpredict the growth of perturbations. Nonlinearity results in mode creation and interaction that leads to the formation of dimples and the tumor surface buckles inwards. The morphologic instability allows the tumor to increase its surface area, relative to its volume, thereby allowing the cells in the tumor bulk greater access to nutrient. This in turn allows the tumor to overcome the diffusional limitations on growth and to grow to larger sizes than would be possible if the tumor were spherical. Consequently, instability provides a means for avascular tumor invasion.

1. **Introduction.** The uncontrolled growth of abnormal cells often results in cancer. Cancer is an enormous societal problem. For example, cancer is newly diagnosed at a rate of every thirty seconds in the United States and is currently the second leading cause of death for adults (after heart disease). In the past thirty-five years, tremendous resources have been spent in understanding and identifying the root causes of cancer and to develop effective treatment strategies. While much progress has been made–roughly 2/3 of people diagnosed with cancer typically live for more than five years– there is much more work to be done to prevent, treat and control or eliminate this complex disease.

In the past several years, the body of research on mathematical models of cancer growth has increased dramatically. See for example the review papers [1, 5, 12, 47, 50, 51]. Most models fall into two categories: discrete cell-based models and continuum models. In discrete modeling, individual cells are tracked and updated according to a specific set of biophysical rules. Examples include cellular automaton modeling (*e.g.*, see [2, 3, 27, 38]), and agent-based models (*e.g.*, [9, 37, 44, 45, 52]). These approaches are particularly useful for studying carcinogenesis, natural selection, genetic instability, and interactions of individual cells with each other and the microenvironment. On the other hand, these methods can be difficult to study analytically, and the computational cost increases rapidly with the number of cells modeled.

In larger-scale systems where the cancer cell population is on the order of 1,000,-000 or more, continuum methods provide a good modeling alternative. The governing equations are typically of reaction-diffusion type. Early work (*e.g.*, [14, 15, 33]), used ordinary differential equations to model cancer as a homogeneous population, as well as partial differential equation models restricted to spherical tumor growth geometries. Linear and weakly nonlinear analysis have been performed to assess the stability of spherical tumors to asymmetric perturbations (*e.g.*, [1, 5, 11, 16]) as a means to characterize the degree of aggression. Reaction-diffusion equations have been successfully used to model brain tumors (*e.g.* glioma, see [36, 39, 51]). Further, various interactions of the tumor with the microenvironment, such as stress-induced limitations of tumor growth, as well as the effects of acidosis, have also been studied

(*e.g.*, [6, 7, 8, 19, 31, 48]). Most of the previous modeling has considered single-phase tumors. Recently, multiphase mixture models have been developed to account for heterogeneities in cell-type and in the mechanical response of the cellular and liquid tumor phases (*e.g.*, [7, 8, 17, 18, 28]).

Very recently, nonlinear modeling has been performed to study the effects of shape instabilities on avascular, vascular and angiogenic solid tumor growth. Cristini *et al.* [26] performed the first fully nonlinear simulations of a continuum model of avascular and vascularized tumor growth in 2-d that accounts for cell-to-cell and cell-to-matrix adhesion. Using a boundary integral method, Cristini *et al.* found that instability provides a mechanism for tumor invasion that does not require an external nutrient source such as would occur from a developing neovasculature during angiogenesis. Zheng *et al.* [54] extended this model to include angiogenesis using a discrete/continuum hybrid model which was originally developed by Anderson *et al.* [4] and investigated the nonlinear coupling between growth and angiogenesis in 2-d using finite element/level-set method. Recently, Hogea *et al.* [34] have also begun investigating tumor growth and angiogenesis using a level set method coupled with a continuous model of angiogenesis.

Using the model developed by Zheng *et al.*, Cristini *et al.* [22] and Frieboes *et al.* [29] examined the competition between heterogeneous cell proliferation, caused by spatial diffusion gradients, and stabilizing mechanical forces, *e.g.* cell-to-cell and cell-to-matrix adhesion. In particular, it is shown that microenvironmental substrate gradients may drive morphologic instability with separation of cell clusters from the tumor edge and infiltration into surrounding normal tissue. Local regions of hypoxia are observed to increase the instability. Macklin and Lowengrub [41, 42, 43] developed a highly accurate level-set/ghost fluid method to further investigate the long-time dynamics and the effect of microenvironmental inhomogeneities on tumor growth in 2-d.

In spite of this recent progress, theory and simulation lag far behind experiments especially in predicting 3-d growth as most numerical methods are 2-d. The work presented in this paper is a step towards closing the gap. Here, we focus on extension to 3-d of the continuum model investigated most recently by Cristini *et al.* [26] in 2D. In particular, we develop a new, adaptive boundary integral method to simulate solid tumor growth in 3-d.

The 3-d problem is considerably more difficult owing to the singularities of the integrals and the 3-d surface geometry. The numerical method relies on accurate discretizations of singular surface integrals, a spatial rescaling and the use of an adaptive surface mesh originally developed by Cristini *et al.* [21]. The discretized boundary integral equations are solved iteratively using GMRES and a discretized version of the Dirichlet-Neumann map is used to determine the normal velocity of the tumor surface. Here, a version of the Dirichlet-Neumann map is used that relies on a vector potential formulation rather than a more standard double-layer potential. The vector potential has the advantage that singularity subtraction can be used to increase the order of accuracy of the numerical quadrature. Explicit time stepping is used to update the tumor surface.

We present simulations of the nonlinear evolution of growing tumors under conditions for which instability is predicted by linear theory. At early times, good agreement is obtained between the linear and nonlinear results. At later times, linear theory is found to overpredict the growth of perturbations. Nonlinearity results in mode creation and interaction that leads to the formation of dimples and the

surface buckles inwards. The morphologic instability allows the tumor to increase its surface area, relative to its volume, thereby allowing the cells in the tumor bulk greater access to nutrient. This is consistent with 2-d observations and allows the tumor to overcome the diffusional limitations on growth and to grow to larger sizes than would be possible if the tumor were spherical. Consequently, as in 2-d, this provides a means for avascular tumor invasion.

Although the mathematical tumor model considered here is highly simplified, this work provides a benchmark to assess the effects of additional biophysical processes not considered here such as necrosis, multiple tumor cell types, tissue stress, angiogenesis and a developing neovasculature as well as other microenvironmental features and inhomogeneities. In addition, the boundary integral results presented here serve as a benchmark for validating other numerical methods, *e.g.* level-set, mixture models, that are capable of simulating more complex biophysical processes.

In section 2, we present the model and the linear stability analysis in three dimensions. In section 3 we present a new boundary integral formulation and its implementation on an adaptive computational mesh. The nonlinear simulations and comparisons to theory are given in Section 4. We conclude this paper in Section 5 with a summary and a brief description of future work.

2. **Problem formulation and linear analysis.**

2.1. **Formulation.** We take $\Omega(t)$ to be the tumor domain, Σ to be the boundary between the tumor tissue and the host tissue, $\mathbf{n}$ to be the unit outward normal vector to Σ and $\mathbf{x}$ to be the position in space. See Fig. 1. We let σ denote the composition of a vital nutrient (*e.g.*, oxygen or glucose). Since the rate of diffusion of oxygen (or glucose) is much faster (*e.g.* ~ 1 minute^{-1}) than the rate of cell-proliferation (*e.g.*, ~ 1 day^{-1}), we may regard the nutrient to be in a steady-state for a given tumor morphology (*e.g.*, [13, 26, 30, 33]). This gives:

$$0 = D\nabla^2\sigma + \Gamma, \tag{1}$$

where Γ is the rate at which nutrient is added to Ω and is given by:

$$\Gamma = -\lambda_B(\sigma - \sigma_B) - \lambda\sigma, \tag{2}$$

where λ_B is the blood-tissue transfer rate of nutrient, σ_B is the concentration of nutrient in the blood, and $\lambda\sigma$ is the rate of consumption of nutrient by the tumor cells.

Following [13, 26, 30, 33] and others, we next assume that in the proliferating tumor domain, the cell-density is constant. Therefore, mass changes correspond to volume changes. Defining $\mathbf{u}$ to be the cell-velocity, the local rate of volume change $\nabla \cdot \mathbf{u}$ is given by:

$$\nabla \cdot \mathbf{u} = \lambda_p, \tag{3}$$

where λ_p is the cell-proliferation rate and λ_p is given by:

$$\lambda_p = b\sigma - \lambda_A, \tag{4}$$

where λ_A is the rate of apoptosis, and b is a measure of mitosis.

To determine the cell velocity , we use Darcy's law as the constitutive assumption (*e.g.*, [13, 26, 30, 32]):

$$\mathbf{u} = -\mu\nabla P, \tag{5}$$

where P is the oncotic (solid) pressure and μ is a mobility that reflects the combined effects of cell-cell and cell-matrix adhesion.

On the tumor interface Σ, the boundary conditions are as follows:

$$(\sigma)_\Sigma = \sigma^\infty, \tag{6}$$
$$(P)_\Sigma = \gamma\kappa, \tag{7}$$

where the pressure boundary condition (7) reflects the influence of cell-cell adhesion through the parameter γ, and κ is the local total curvature. For simplicity, here we assume σ^∞ is constant so that outside the tumor, the nutrient is uniform. Nutrient inhomogeneity in the tumor microenvironment in 2-d has been considered in [22, 29, 42, 43, 54]. We will consider inhomogeneity in 3-d in a future work.

The normal velocity $V = \mathbf{n}\cdot(\mathbf{u})_\Sigma$ of the tumor boundary is

$$V = -\mu\mathbf{n}\cdot(\nabla P)_\Sigma. \tag{8}$$

Following [13, 26, 30, 32] and others, we assume that λ, λ_B, σ_B, b are uniform. Following [26], we denote $\lambda_M = b\sigma^\infty$ to be the characteristic mitosis rate, $\lambda_R = \mu\gamma L_D^{-3}$ to be the intrinsic relaxation time scale, and $B = \sigma_B\lambda_B/\sigma^\infty(\lambda_B+\lambda)$ to be a measure of the extent of vascularization. Introducing the nondimensional length scale $L_D = D^{\frac{1}{2}}(\lambda_B+\lambda)^{-\frac{1}{2}}$, time scale λ_R^{-1} and then define a modified concentration $\bar\Gamma$ and pressure $\bar p$ by [26]:

$$\begin{aligned}\sigma &= \sigma^\infty(1-(1-B)(1-\bar\Gamma)),\\ P &= \frac{\gamma}{L_D}(\bar p + (1-\bar\Gamma)G + AG\frac{\mathbf{x}\cdot\mathbf{x}}{6}),\end{aligned} \tag{9}$$

where G and A measure the relative strength of cell-cell and cell-matrix adhesion and apoptosis respectively:

$$\begin{aligned}G &= \frac{\lambda_M}{\lambda_R}(1-B),\\ A &= \frac{\lambda_A/\lambda_M - B}{1-B}.\end{aligned} \tag{10}$$

Next, dropping all the bars, we obtain the nondimensional equations for Γ and p:

$$\nabla^2\Gamma - \Gamma = 0, \tag{11}$$
$$\nabla^2 p = 0, \tag{12}$$
$$\tag{13}$$

with boundary conditions:

$$(\Gamma)_\Sigma = 1, \tag{14}$$
$$(p)_\Sigma = \kappa - AG\frac{(\mathbf{x}\cdot\mathbf{x})_\Sigma}{6}. \tag{15}$$

Finally, the tumor surface is evolved using the normal velocity

$$V = -\mathbf{n}\cdot(\nabla p)_\Sigma + G\mathbf{n}\cdot(\nabla\Gamma)_\Sigma - AG\frac{\mathbf{n}\cdot(\mathbf{x})_\Sigma}{3}. \tag{16}$$

2.2. **Linear Analysis.** A growing or shrinking spherical tumor is an exact solution of Eqns. (11)-(16). In [26], Cristini et. al. analyzed the linear stability of perturbed spherical tumors. Here, for completeness we summarize their results.

We consider a perturbation of the spherical tumor interface Σ:

$$r(\theta,\phi,t) = R(t) + \delta(t)Y_{l,m}(\theta,\phi), \tag{17}$$

where r is the radius of the perturbed sphere, R is the radius of the underlying sphere, δ is the dimensionless perturbation size and $Y_{l,m}$ is a spherical harmonic, l and θ are the polar wavenumber and angle, and m and ϕ are the azimuthal wavenumber and angle.

It can be shown that the evolution equation for the tumor radius R is given by [26]:

$$\frac{dR}{dt} = V = -AG\frac{R}{3} + G\left(\frac{1}{\tanh(R)} - \frac{1}{R}\right) \tag{18}$$

and the equation for the shape perturbation δ/R is given by [26]:

$$\begin{aligned}(\frac{\delta}{R})^{-1}\frac{d(\frac{\delta}{R})}{dt} &= G - \frac{l(l+2)(l-1)}{R^3} - G\frac{l+3}{R}(\frac{1}{\tanh(R)} - \frac{1}{R}) \\ &\quad -G\frac{I_{l+\frac{3}{2}}(R)}{I_{l+\frac{1}{2}}(R)}(\frac{1}{\tanh(R)} - \frac{1}{R}) + l\frac{AG}{3},\end{aligned} \tag{19}$$

where $I_{l+\frac{3}{2}}(R)$ and $I_{l+\frac{1}{2}}(R)$ are the modified Bessel functions of the first kind. In [26], this formula was incorrectly stated as the 4^{th} term on the right-hand-side was omitted. A complete derivation and description is given in [40] and [23].

At the level of linear theory, perturbations consisting of different spherical harmonics are superpositions of the above solutions. Observe that the shape perturbation depends on l but not on m.

Fig. 2(a) shows the rescaled rate of growth V/G as a function of rescaled tumor radius R for radially symmetric tumor growth. For given A, evolution from initial condition $R(0) = R_0$ occurs along the corresponding curve. Fig. 2(b) characterizes the stability region by keeping G constant and varying A as a function of the unperturbed radius R. By setting $\frac{d}{dt}(\delta/R) = 0$ identically in Eqn. (19), we obtain

$$\begin{aligned}A_c &= \frac{3(l-1)(l+2)}{GR^3} - \frac{3}{l} + 3(1+\frac{3}{l})\frac{1}{R}(\frac{1}{\tanh(R)} - \frac{1}{R}) \\ &\quad +\frac{3}{l}\frac{I_{l+\frac{3}{2}}(R)}{I_{l+\frac{1}{2}}(R)}(\frac{1}{\tanh(R)} - \frac{1}{R}),\end{aligned} \tag{20}$$

where A_c is the critical value which divides the plot into regions of stable growth (region $A < A_c$ (i.e. below the curve) for $G > 0$ and the region $A > A_c$ for $G < 0$) and regions of unstable growth (region $A > A_c$ for $G > 0$ and the region $A < A_c$ for $G < 0$) of a given mode l.

It can be shown that, the limiting behavior of A_c as $l \to \infty$ is given by:

$$A_c \to \frac{3(l-1)(l+2)}{GR^3}. \tag{21}$$

As described in [26], three growth regimes are identified via the parameters A and G. These are given as follows.

Low vascularization: $G \geq 0$ and $A > 0$. In this regime, evolution is monotonic and always leads to a stationary state R_∞. We note that $R_\infty > 0$ only if $0 < A < 1$, i.e., if $A \geq 1$, then $R_\infty = 0$. Unstable growth may occur and is possible *only* in this regime. Instability arises because growth is limited by diffusion of nutrient (*e.g.*, Diffusional instability). This is analogous to the Mullins-Sekerka diffusional instability that occurs in crystal growth [24, 25, 46].

Moderate vascularization: $G \geq 0$ and $A \leq 0$. Unbounded growth occurs from any initial radius $R_0 > 0$. The growth tends to become exponential in time for $A < 0$

and to linear for $A = 0$. During unbounded growth, $AG \leq 0$ and perturbations decay to zero since $(\delta/R)^{-1}d(\delta/R)/dt \to lAG/3 < 0$ for $R \to \infty$.

High vascularization: $G < 0$. For $A > 0$, depending on the initial radius, the evolution may lead to stationary state $R_\infty = 0$ or unbounded growth which is always stable as $R \to \infty$. For $A < 0$, the evolution tends always to the only stationary solution $R_\infty = 0$, unstable shrinkage may occur in this regime.

In what follows, we will focus on the low vascularization regime. More specifically, we will study unstable growth in this regime.

3. Numerical Method.

3.1. Boundary Integral Formulation.

From potential theory, the nondimensional nutrient concentration Γ can be expressed using a single-layer potential μ [53]:

$$\Gamma(\mathbf{x}) = \frac{1}{4\pi}\int_\Sigma \mu(\mathbf{x}')\frac{e^{-|\mathbf{x}'-\mathbf{x}|}}{|\mathbf{x}'-\mathbf{x}|}d\Sigma(\mathbf{x}'). \tag{22}$$

Taking the limit of Eqn. (22) as $\mathbf{x}$ approaches the interface along with the boundary condition for Γ from Eqn. (22) gives a first-kind Fredholm integral equation for μ:

$$1 = \frac{1}{4\pi}\int_\Sigma \mu(\mathbf{x}')\frac{e^{-|\mathbf{x}'-\mathbf{x}|}}{|\mathbf{x}'-\mathbf{x}|}d\Sigma(\mathbf{x}'). \tag{23}$$

The normal derivative of Γ can be computed via the Dirichlet-Neumann map [20]:

$$\begin{aligned}\frac{\partial\Gamma}{\partial\mathbf{n}}(\mathbf{x}) &= \frac{1}{4\pi}\fint_\Sigma \mu(\mathbf{x}')e^{-|\mathbf{x}'-\mathbf{x}|}\Big(\frac{|\mathbf{x}'-\mathbf{x}|+1}{|\mathbf{x}'-\mathbf{x}|^3}\Big)(\mathbf{x}'-\mathbf{x})\cdot\mathbf{n}(\mathbf{x})d\Sigma(\mathbf{x}') \\ &\quad +\frac{\mu(\mathbf{x})}{2},\end{aligned} \tag{24}$$

where $\fint$ denotes the principal-valued integral.

For the computation of the modified pressure p, we first represent p using a double-layer potential ν [53]:

$$p(\mathbf{x}) = \frac{1}{4\pi}\fint_\Sigma \nu(\mathbf{x}')\frac{(\mathbf{x}'-\mathbf{x})\cdot\mathbf{n}(\mathbf{x}')}{|\mathbf{x}'-\mathbf{x}|^3}d\Sigma(\mathbf{x}'). \tag{25}$$

Then making use of the following identity for a closed surface Σ:

$$\frac{1}{4\pi}\fint_\Sigma \frac{(\mathbf{x}'-\mathbf{x})\cdot\mathbf{n}(\mathbf{x}')}{|\mathbf{x}'-\mathbf{x}|^3}d\Sigma(\mathbf{x}') = \frac{1}{2}, \tag{26}$$

we recast Eqns. (12) and (15) for p in terms of the second-kind Fredholm integral equation for ν [53]:

$$\kappa - \frac{AG}{6}|\mathbf{x}|^2 = \nu(\mathbf{x}) + \frac{1}{4\pi}\int_\Sigma (\nu(\mathbf{x}')-\nu(\mathbf{x}))\frac{(\mathbf{x}'-\mathbf{x})\cdot\mathbf{n}(\mathbf{x}')}{|\mathbf{x}'-\mathbf{x}|^3}d\Sigma(\mathbf{x}'), \tag{27}$$

note that the singularity in the integrand is now integrable.

The normal derivative of p is computed by representing the solenoidal vector field ∇p in terms of a vector potential $\mathbf{A}$ (*e.g.*, [35]):

$$\nabla p = \nabla\times\mathbf{A}. \tag{28}$$

It can be shown that $\mathbf{A}$ is given by:

$$\mathbf{A}(\mathbf{x}) = \frac{1}{4\pi}\fint_\Sigma \nu(\mathbf{x}')\frac{(\mathbf{x}'-\mathbf{x})\times\mathbf{n}(\mathbf{x}')}{|\mathbf{x}'-\mathbf{x}|^3}d\Sigma(\mathbf{x}'). \tag{29}$$

One advantage of using vector potential formulation is that the following identity holds

$$\frac{1}{4\pi}\not\int_{\Sigma} \frac{(\mathbf{x}'-\mathbf{x})\times\mathbf{n}(\mathbf{x}')}{|\mathbf{x}'-\mathbf{x}|^3}d\Sigma(\mathbf{x}') = 0. \tag{30}$$

This can be used to reduce the order of the singularity in the integrand in the vector potential via singularity subtraction. The vector potential can thus be calculated by:

$$\mathbf{A}(\mathbf{x}) = \frac{1}{4\pi}\int_{\Sigma}(\nu(\mathbf{x}')-\nu(\mathbf{x}))\frac{(\mathbf{x}'-\mathbf{x})\times\mathbf{n}(\mathbf{x}')}{|\mathbf{x}'-\mathbf{x}|^3}d\Sigma(\mathbf{x}'), \tag{31}$$

where the integrand is now integrable. The normal derivative of pressure is then calculated in terms of $\mathbf{A}$ by:

$$\frac{\partial p}{\partial \mathbf{n}} = \mathbf{n}\cdot(\nabla\times\mathbf{A}), \tag{32}$$

which is a form of the Dirichlet-Neumann map for Laplace's equation.

3.2. **Spatial Rescaling.** In order to enhance the accuracy of the numerical method, we found it useful to rescale the dimensionless formulation in space by introducing a time-dependent growth factor $\mathcal{S}(t)$ that transforms the position $\mathbf{x}$ according to

$$\mathbf{x} = \mathcal{S}(t)\tilde{\mathbf{x}}, \tag{33}$$

such that the tumor volume in the new spatial variable $\tilde{\mathbf{x}}$ is time-independent. The domain Ω and interface Σ accordingly are transformed by a multiplicative factor of $\mathcal{S}(t)$ to $\tilde{\Omega}$ and $\tilde{\Sigma}$ respectively.

Letting $\tilde{p}(\tilde{\mathbf{x}}) = p(\mathbf{x}(\tilde{\mathbf{x}}))$, $\tilde{\Gamma}(\tilde{\mathbf{x}}) = \Gamma(\mathbf{x}(\tilde{\mathbf{x}}))$, and using analogous notation for the other variables, the rescaled equations are as follows

$$0 = \tilde{\nabla}^2\tilde{\Gamma} - \mathcal{S}^2\tilde{\Gamma}, \tag{34}$$

$$0 = \tilde{\nabla}^2\tilde{p}, \tag{35}$$

with boundary conditions

$$(\tilde{\Gamma})_{\tilde{\Sigma}} = 1, \tag{36}$$

$$(\tilde{p})_{\tilde{\Sigma}} = \frac{\tilde{\kappa}}{\mathcal{S}} - \frac{AG}{6}\mathcal{S}^2|\tilde{\mathbf{x}}|^2, \tag{37}$$

where $\mathcal{S}^2\nabla^2 = \tilde{\nabla}^2$, and $\mathcal{S}\kappa = \tilde{\kappa}$.

The normal velocity is computed by

$$\tilde{V} = -\frac{\mathcal{S}'}{\mathcal{S}}(\tilde{\mathbf{x}}\cdot\tilde{\mathbf{n}})_{\tilde{\Sigma}} + \frac{1}{\mathcal{S}^2}\left(G\frac{\partial\tilde{\Gamma}}{\partial\tilde{\mathbf{n}}} - \frac{\partial\tilde{p}}{\partial\tilde{\mathbf{n}}}\right)_{\tilde{\Sigma}} - \frac{AG}{3}(\tilde{\mathbf{x}}\cdot\tilde{\mathbf{n}})_{\tilde{\Sigma}}. \tag{38}$$

Since the scale factor $\mathcal{S}(t)$ is chosen such that the tumor volume in the rescaled coordinate does not change in time, we have

$$\int_{\tilde{\Sigma}}\tilde{V}d\Sigma = 0. \tag{39}$$

From (39) and (38), a calculation shows that $\mathcal{S}(t)$ satisfies the following differential equation:

$$3\mathcal{S}'(t) = \frac{G}{\mathcal{S}(t)|\tilde{\Omega}|}\int_{\tilde{\Sigma}}\frac{\partial\tilde{\Gamma}}{\partial\tilde{\mathbf{n}}}d\Sigma - AG\mathcal{S}(t). \tag{40}$$

Next, we drop all the tildes and assume in the remainder of the paper that all the variables are scaled. The boundary integral equations for the nutrient concentration and pressure are then:

$$1 = \frac{1}{4\pi}\int_\Sigma \mu(\mathbf{x}')\frac{e^{-\mathcal{S}|\mathbf{x}'-\mathbf{x}|}}{|\mathbf{x}'-\mathbf{x}|}d\Sigma(\mathbf{x}'), \tag{41}$$

$$\frac{\kappa}{\mathcal{S}} - \frac{AG}{6}\mathcal{S}^2|\mathbf{x}|^2 = \nu(\mathbf{x}) + \frac{1}{4\pi}\int_\Sigma (\nu(\mathbf{x}')-\nu(\mathbf{x}))\frac{(\mathbf{x}'-\mathbf{x})\cdot\mathbf{n}(\mathbf{x}')}{|\mathbf{x}'-\mathbf{x}|^3}d\Sigma(\mathbf{x}'). \tag{42}$$

The normal derivative of Γ and p can be calculated analogously using Eqns. (24) and (32).

3.3. **Numerical Implementation.** We briefly describe the procedure to evolve the tumor surface Σ in time. Initially, the tumor surface $\Sigma(0)$ is given. The surface is then discretized into a mesh of flat triangles and the scaling factor $\mathcal{S}(0)$ is set to be the initial effective tumor radius making the scaled interface have effective radius equal to 1. The effective radius is defined to be the radius of a sphere enclosing the same volume. The following steps are implemented: (1) calculate the scaling factor $\mathcal{S}(t)$ from Eqn. (40); (2) compute ν by solving Eqn. (42) iteratively using the Generalized Minimum Residual (GMRES) method [49]; (3) compute the vector potential $\mathbf{A}$ using Eqn. (31); (4) compute $\partial p/\partial \mathbf{n} = (\nabla\times\mathbf{A})\cdot\mathbf{n}$; (5) Solve Eqn. (41) for μ using GMRES; (6) compute $\partial\Gamma/\partial\mathbf{n}$ using Eqn. (24); (7) assemble the normal velocity V from steps (4) and (6); (8) evolve the tumor surface using $V = \mathbf{n}\cdot(d\mathbf{x}/dt)$ by an explicit 2^{nd} order Runge-Kutta time stepping method; (9) remesh the surface according to the criteria discussed below, and finally repeat the entire process starting from step (1).

3.3.1. *The Pressure Boundary Integral Equation.* As mentioned above, the discretized form of Eqn. (42) is solved using GMRES. Due to the singularity of the integrand, the discretization of the integrand must be done with care to achieve accurate results. To discretize the integral, we divide the triangulation of Σ into non-singular and singular triangles. The singular triangles have a vertex that corresponds to the evaluation point $\mathbf{x}$. The integration over the non-singular triangles is performed using the Trapezoidal rule. Integration over the singular triangles is performed using a different quadrature rule that is capable of handling the singular integrand. Suppose Δ is a singular triangle with vertices $\mathbf{x}_1$, $\mathbf{x}_2$ and $\mathbf{x}_3$. Let $\mathbf{x}'$ be an interior point of Δ, then we can write

$$\mathbf{x}' = \mathbf{x}_1 + s(\mathbf{x}_2-\mathbf{x}_1) + t(\mathbf{x}_3-\mathbf{x}_1) = \mathbf{x}_1 + s\mathbf{x}_{21} + t\mathbf{x}_{31}, \tag{43}$$

where $\mathbf{x}_{21} = \mathbf{x}_2 - \mathbf{x}_1$ (likewise for $\mathbf{x}_{31}$), and (s,t) belongs to the standard right triangle in the xy-plane with vertices $(0,0)$, $(1,0)$, and $(0,1)$. The values of ν and $\mathbf{n}$ can be linearly interpolated into the interior of Δ by

$$\nu(s,t) = \nu_1 + s\nu_{21} + t\nu_{31}, \qquad \mathbf{n}(s,t) = \mathbf{n}_1 + s\mathbf{n}_{21} + t\mathbf{n}_{31}. \tag{44}$$

We then apply Duffy's transformation [10]:

$$s = (1-\eta)\xi, \qquad t = \eta\xi, \tag{45}$$

and transform the integral (42) over Δ to

$$\frac{\text{Area}(\Delta)}{2\pi}\int_0^1\int_0^1 (\nu_{21}+\eta\nu_{32})\frac{(\mathbf{x}_{21}+\eta\mathbf{x}_{32})\cdot(\mathbf{n}_1+\xi(\mathbf{n}_{21}+\eta\mathbf{n}_{32}))}{|\mathbf{x}_{21}+\eta\mathbf{x}_{32}|^3\cdot|\mathbf{n}_1+\xi(\mathbf{n}_{21}+\eta\mathbf{n}_{32})|}d\eta d\xi. \tag{46}$$

The integrand is non-singular and we can apply the Trapezoidal rule to perform the integration.

3.3.2. *The Nutrient Boundary Integral Equation.* Before describing the discretization, we first present a reformulation of the equation that will prove to be useful later when we calculate $\partial\Gamma/\partial\mathbf{n}$.

We define a new nutrient concentration $\bar{\Gamma}$ such that

$$\bar{\Gamma} = \Gamma - \Gamma^{sph}, \tag{47}$$

where Γ^{sph} is the solution to Eqns. (34), (36) on a sphere. Note that

$$\Gamma^{sph} = \frac{\mathcal{S}}{\sinh(\mathcal{S})}\frac{\sinh(\mathcal{S}r)}{\mathcal{S}r}. \tag{48}$$

We then reformulate the boundary integral equation (41) for a single layer potential $\bar{\mu}$ satisfying

$$1 - \Gamma^{sph} = \frac{1}{4\pi}\int_{\bar{\Sigma}} \bar{\mu}(\mathbf{x}')\frac{e^{-\mathcal{S}|\mathbf{x}'-\mathbf{x}|}}{|\mathbf{x}'-\mathbf{x}|}d\Sigma(\mathbf{x}'). \tag{49}$$

When the shape of the tumor is close to a sphere, $\bar{\mu} \approx 0$. It turns out that even when Ω is non-spherical, Γ^{sph} contains the dominant part of the solution and $\bar{\mu}$ remains fairly small.

To evaluate the integrand in Eqn. (49), care must be taken because of the (integrable) singularity of the integrand and the fact that as $\mathcal{S}$ increases, the kernel is more localized. We develop a scheme to evaluate the integral by first dividing the discretized tumor surface into three regions: (i) a singular region which contains all triangles with the evaluation point $\mathbf{x}$ as a vertex; (ii) a quasi-singular region which is the collection of triangles whose center is some distance d from $\mathbf{x}$; and (iii) a non-singular region which contains all other triangles. The quasi-singular region is the set

$$\left\{\Delta | \frac{e^{-\mathcal{S}d}}{d} > \epsilon \text{ where } d = dist(\Delta_c, \mathbf{x})\right\}, \tag{50}$$

where ϵ is a user-defined tolerance, Δ_c is the center of the triangle Δ and $\mathbf{x}$ is the evaluation point. In the non-singular region, we use the Trapezoidal rule to perform the integration. For a triangle Δ in the quasi-singular region, we transform the triangle Δ to the standard right triangle as in the previous subsection, and the value of the function $\bar{\mu}$ is linearly interpolated into the interior of Δ. Then the integral is evaluated accurately using the seven-point Gaussian quadrature rule. Here, Gaussian quadrature is used instead of the Trapezoidal rule to more accurately resolve the exponential term in the integrand. For the singular contribution, Duffy's transformation is used to map the standard right triangle to a unit square. The the square is then split into two non-intersecting triangles and the integral is discretized using the seven-point Gaussian quadrature rule on each triangle. Finally, GMRES is used to solve Eqn. (49) iteratively. We note that although Eqn. (49) is a first-kind Fredholm integral equation and hence is subject to numerical instability, we are nevertheless able to obtain accurate solutions because the right hand side is known analytically. Consequently, there is little error from the right hand side that can be amplified.

3.3.3. *The normal derivatives.* The normal derivative $\partial\Gamma/\partial\mathbf{n}$ can be calculated as

$$\frac{\partial\Gamma}{\partial\mathbf{n}} = \frac{\partial\bar{\Gamma}}{\partial\mathbf{n}} + \frac{\mathcal{S}}{\sinh(\mathcal{S})}\Big(\frac{\cosh(\mathcal{S}r)}{r} - \frac{\sinh(\mathcal{S}r)}{\mathcal{S}r^2}\Big)\frac{\mathbf{x}\cdot\mathbf{n}}{r}, \tag{51}$$

where $\partial\bar{\Gamma}/\partial\mathbf{n}$ is given by

$$\frac{\partial\bar{\Gamma}}{\partial\mathbf{n}} = \frac{1}{4\pi}\not\int_{\Sigma} \bar{\mu}(\mathbf{x}')e^{-\mathcal{S}|\mathbf{x}'-\mathbf{x}|}\Big(\frac{\mathcal{S}|\mathbf{x}'-\mathbf{x}|+1}{|\mathbf{x}'-\mathbf{x}|^3}\Big)(\mathbf{x}'-\mathbf{x})\cdot\mathbf{n}(\mathbf{x})d\Sigma + \frac{\bar{\mu}(\mathbf{x})}{2}. \tag{52}$$

We write

$$\frac{\partial\Gamma}{\partial\mathbf{n}} = \mathcal{S}I_1 - I_2 - I_3 + I_4 + \frac{\bar{\mu}}{2}, \tag{53}$$

where

$$I_1 = \frac{1}{4\pi}\int_{\Sigma} \bar{\mu}(\mathbf{x}')e^{-\mathcal{S}|\mathbf{x}'-\mathbf{x}|}\frac{(\mathbf{x}'-\mathbf{x})\cdot\mathbf{n}(\mathbf{x})}{|\mathbf{x}'-\mathbf{x}|^2}d\Sigma, \tag{54}$$

$$I_2 = \frac{1}{4\pi}\int_{\Sigma} \bar{\mu}(\mathbf{x}')e^{-\mathcal{S}|\mathbf{x}'-\mathbf{x}|}\frac{(\mathbf{x}'-\mathbf{x})\cdot(\mathbf{n}(\mathbf{x}')-\mathbf{n}(\mathbf{x}))}{|\mathbf{x}'-\mathbf{x}|^3}d\Sigma, \tag{55}$$

$$I_3 = \frac{1}{4\pi}\int_{\Sigma} \bar{\mu}(\mathbf{x}')(1-e^{-\mathcal{S}|\mathbf{x}'-\mathbf{x}|})\frac{(\mathbf{x}'-\mathbf{x})\cdot\mathbf{n}(\mathbf{x}')}{|\mathbf{x}'-\mathbf{x}|^3}d\Sigma, \tag{56}$$

$$I_4 = \frac{1}{4\pi}\int_{\Sigma} (\bar{\mu}(\mathbf{x}')-\bar{\mu}(\mathbf{x}))\frac{(\mathbf{x}'-\mathbf{x})\cdot\mathbf{n}(\mathbf{x}')}{|\mathbf{x}'-\mathbf{x}|^3}d\Sigma. \tag{57}$$

The evaluation of I_4 is given in section 3.3.1 with ν replaced by $\bar{\mu}$. To evaluate the integrals I_1, I_2 and I_3, we use an analogous strategy to that used to discretize the single layer potential in Eqn. (49).

To evaluate $\partial p/\partial\mathbf{n}$, we first discretize the vector potential in Eqn. (31) in a way similar to the scalar potential in Eqn. (42) with the dot product replaced by cross product. Once $\mathbf{A}$ is determined at the node points, we calculate $\nabla\times\mathbf{A}$ using a least-squares parabolic fit of $\mathbf{A}$. In particular, at a node point $\mathbf{x}$ with neighboring node points $\mathbf{x}'$, we create a local co-ordinate system which transforms $\mathbf{x}$ to the origin, and $\mathbf{x}'$ into $\tilde{\mathbf{x}}'$. We then get

$$\mathbf{A}(\mathbf{x}) \approx \mathbf{a} + \mathbf{b}\tilde{x}' + \mathbf{c}\tilde{y}' + \mathbf{d}\tilde{x}'\tilde{y}' + \mathbf{e}\tilde{x}'^2 + \mathbf{f}\tilde{y}'^2. \tag{58}$$

Therefore $(\nabla\times\mathbf{A})\cdot\mathbf{n}$ at $\mathbf{x}$ is approximated by

$$[\nabla\times\mathbf{A}]\cdot\mathbf{n} \approx a_2 - b_1, \tag{59}$$

where a_2 and b_1 are the second and first components of the vectors $\mathbf{a}$ and $\mathbf{b}$ respectively.

3.3.4. *Time Stepping.* The tumor surface is evolved by an explicit 2^{nd} order Runge-Kutta time stepping method. We impose a time step restriction $\Delta t \sim h^2$ for stability where h is the minimum edge length of the surface triangulation.

3.3.5. *Mesh Adaptivity.* We use an efficient adaptive surface mesh algorithm that was recently developed by Cristini *et al.* [21]. In this algorithm, the surface is represented by a mesh of flat triangles. The mesh is independent of the biophysics and is adapted to resolve the relevant local length scales. Here, we essentially use the minimum radius of the curvature as the local length scale. Consequently, mesh points cluster in regions where the curvature is large in absolute value. We note that other criteria have been used (*e.g.*, [21]).

The mesh is adapted by minimizing a spring-like mesh energy function by local operations: equilibration, node addition/subtraction, and edge-swapping. Using

the adaptive mesh, complex evolving shapes are resolved accurately and efficiently making accurate long time simulations possible.

Although the mesh triangles are flat, other geometric properties such as the normal vector and the curvature of each node point are calculated more accurately using a local paraboloid fit [55]. Thus the discrete representation of the surface is first-order accurate with the total number of node points used to represent the interface.

4. **Results.** Here, we investigate the nonlinear, unstable evolution of 3-d tumors in the low-vascularization regime characterized by $G \geq 0$ and $A > 0$. We focus on the parameters $G = 20$ and $A = 0.5$. Note that a spherical tumor with these parameters reaches a steady-state with corresponding scale factor $\mathcal{S} = 4.73$. We consider the evolution using three different initial conditions.

In Fig 3, the morphological evolution of a tumor is shown from the initial radius

$$r = 1 + 0.033\, Y_{2,2}(\theta, \phi), \tag{60}$$

with the initial scale factor $\mathcal{S}(0) = 3.002$. Two 3-d views of the morphology are shown, as indicated. Because of the spatial rescaling, the tumor does not change volume in the simulation as seen in the figure. The associated evolution of the scale factor $\mathcal{S}(t)$ is shown in Fig. 4(a).

At early times, the perturbation decreases and the tumor becomes sphere-like. As the tumor continues to grows, the perturbation starts to increase around time $t \approx 0.4$ when the scale factor $\mathcal{S} \approx 3.7$. The tumor then takes on a flattened ellipse-like shape. Around time $t \approx 2.2$, when $\mathcal{S} \approx 4.6$, the perturbation growth accelerates dramatically and dimples form around time $t \approx 2.42$. The dimples deepen and the tumor surface buckles inwards. The instability and dimple formation allows the tumor to increase its surface area, relative to its volume, thereby allowing the cells in the tumor bulk greater access to nutrient. This in turn allows the tumor to overcome the diffusional limitations on growth and to grow to larger sizes than would be possible if the tumor were spherical. For example, in Fig. 3(d), the scale factor $\mathcal{S} \approx 4.78$ which is larger than the corresponding value (4.73) for the steady-state spherical tumor. (Note that the tumor is continuing to grow.) This provides additional support in 3-d for the hypothesis put forth by Cristini *et al.* [22, 26, 29], based on 2-d simulations, that morphologic instability allows an additional pathway for tumor invasion that does not require an additional nutrient source such as would be provided from a newly developing vasculature through angiogenesis.

In this simulation, the number of mesh points is $N = 1024$ initially. As seen in Fig. 3, the mesh adaptively clusters near the dimples where there is large negative curvature thereby providing enhanced local resolution. At the final time $t_f = 2.67$ (with $\mathcal{S} \approx 4.78$) there are $N = 2439$ nodes on the tumor surface. To compute for longer times, higher resolution is necessary.

We next compare the nonlinear results with the predictions of linear theory. To estimate the shape perturbation size $\bar{\delta}$ in the nonlinear simulation, which is compared to the linear prediction δ/R from Eqn. (19), we take

$$\bar{\delta} = \max_{\Sigma} |r_\Sigma - 1| \tag{61}$$

since the overall bulk growth is scaled out of the nonlinear evolution by the scale factor $\mathcal{S}(t)$.

In Fig. 4(b), the results of linear theory (solid) and nonlinear simulations (dashed-dot) for the perturbation size are shown as functions of $S(t)$ for the evolution from Fig. 3. Linear theory predicts that, for $G = 20$, $A = 0.5$, the 2-mode is stable for $\mathcal{S} < 3.54$. This is borne out by the nonlinear simulation which agrees very well with the linear theory up until $\mathcal{S} \approx 3.5$ where the linear theory predicts the perturbation starts to grow. In the nonlinear simulation, the perturbation continues to decay until $\mathcal{S} \approx 3.7$. Although the linear and nonlinear results deviate at larger $\mathcal{S}$ with linear theory predicting larger perturbations, the qualitative behavior of the shape perturbation is very similar in both cases. In particular, there is rapid growth of the perturbation near $R \approx 4.6$. The circled points labeled A-D on the dashed-dot curve (nonlinear simulation) correspond to the morphologies shown in Figs. 3(a)-(d). Note that at the final time, the nonlinear perturbation $\bar{\delta} \approx 0.5$ and so the evolution is highly nonlinear.

In Figs. 4(c) and (d), the nonlinear and linear tumor morphologies, respectively, are shown at time $t = 2.668$ where $\mathcal{S} \approx 4.78$ and $\mathcal{S}_{\text{linear}} \approx 4.73$. The linear morphology is generated by evolving a sphere to the shape prescribed by linear theory. This is why the linear solution is shown with a triangulated mesh. The corresponding nonlinear and linear perturbation sizes are $\bar{\delta} = 0.496$ and $\delta/R = 0.42$ respectively. We note that the reason the linear result is smaller than the nonlinear value at this time is because the linear scale factor is slightly less than that from the nonlinear simulation which, when combined with the rapid growth of the perturbation around $\mathcal{S} \approx 4.76$, gives rise to this behavior.

As seen in Figs. 4(c) and (d), the nonlinear tumor morphology is more compact than the corresponding linear result. In fact, the linear perturbation eventually grows so large that the tumor pinches off in the center. In contrast, nonlinearity introduces additional modes that alter the growth directions, from primarily horizontal in Fig. 4(d) to more vertical in Fig. 4(c), thereby avoiding pinchoff and resulting in more compact shapes. This is consistent with the 2-d results of Cristini *et al.* [26].

In Figs. 5 and 7 the morphological evolution is shown of tumors evolving from different initial radii

$$r = 1 + 0.033\ Y_{3,1}(\theta, \phi),\ \mathcal{S} = 3.0025, \tag{62}$$

and

$$r = 1 + 0.033 Y_{3,2}(\theta, \phi),\ \mathcal{S} = 3.0025, \tag{63}$$

respectively. As before, two 3-d views of the morphology are shown. Qualitatively, the evolution is similar to that obtained for the initial radius given in Eq. (60). At early times, the perturbation decays and the tumor becomes sphere-like. At later times, the perturbation grows and a 3-fold shape emerges. The sides flatten and dimples form and deepen yielding complex tumor morphologies. In each case, the tumor grows larger than the spherical steady-state. See Figs. 6(a) and 8(a). In both simulations, $N = 1024$ initially and increases to $N = 2556$ and to $N = 2346$ at the final times shown in Figs. 5 and 7 respectively.

Comparisons with linear theory are shown in Figs. 6(b)-(d) and 8(b)-(d). For $G = 20$ and $A = 0.5$, linear theory predicts that the 3-mode becomes unstable at $R \approx 3.58$. As before, there is good agreement between the linear and nonlinear results for small $\mathcal{S}$ (i.e. up to $\mathcal{S} \approx 3.5$). However, compared to the 2-mode results, deviations between linear and nonlinear results occur at somewhat smaller $\mathcal{S}$ as the nonlinearity decreases the amplitude of the perturbation. Comparing the linear and

nonlinear tumor morphologies at the same time, it is seen that the linear solution has a more complex shape.

5. **Conclusions.** We developed a new, adaptive boundary integral method to simulate solid tumor growth in 3-d. We used a reformulation of a classical model [13, 26, 30, 33] that accounts for cell-proliferation, apoptosis, cell-to-cell and cell-to matrix adhesion. This is an extension to 3-d of the work by Cristini *et al.* [26] who studied nonlinear evolution in 2-d using this model. The 3-d problem is considerably more difficult owing to the singularities of the surface integrals and the 3-d surface geometry. The 3-d method relied on accurate discretizations of singular surface integrals, a spatial rescaling and the use of an adaptive surface mesh originally developed by Cristini *et al.* [21]. The discretized boundary integral equations are solved iteratively using GMRES and a discretized version of the Dirichlet-Neumann map is used to determine the normal velocity of the tumor surface. Here, a version of the Dirichlet-Neumann map is used that relies on a vector potential formulation rather than a more standard double-layer potential. The vector potential has the advantage that singularity subtraction can be used to increase the order of accuracy of the numerical quadrature. Explicit time stepping is used to update the tumor surface.

We performed simulations of the nonlinear evolution of growing tumors under conditions for which instability was predicted by linear theory. At early times, good agreement was obtained between the linear and nonlinear results. At later times, linear theory was found to overpredict the growth of perturbations. Nonlinearity results in mode creation and interaction that leads to the formation of dimples and the surface buckles inwards. The morphologic instability allows the tumor to increase its surface area, relative to its volume, thereby allowing the cells in the tumor bulk greater access to nutrient. This in turn allows the tumor to overcome the diffusional limitations on growth and to grow to larger sizes than would be possible if the tumor were spherical. This provides additional support in 3-d for the hypothesis put forth by Cristini *et al.* [22, 26, 29], based on 2-d simulations, that morphologic instability allows an additional pathway for avascular tumor invasion.

Although the mathematical tumor model considered here is highly simplified, this work provides a benchmark to assess the effects of additional biophysical processes not considered here such as necrosis, multiple tumor cell types, angiogenesis and a developing neovasculature as well as other microenvironmental features and inhomogeneities. In addition, the boundary integral results presented here serve as a benchmark for validating other numerical methods, *e.g.* level-set, mixture models, that are capable of simulating more complex biophysical processes. A number of such models and numerical methods have been developed in 2-d (*e.g.*, see [22, 28, 29, 42, 43, 54]); we are currently developing extensions of such models and methods to 3-d [23, 28].

Acknowledgements. The authors thank Dr. Lan Pham for valuable contributions to the early stages of this work. The authors also thank UROP student Genevieve Brown and Drs. Shuwang Li and Xiaoming Zheng for useful discussions. XL and JSL acknowledge partial support from the National Science Foundation (NSF) through grants DMS-0352143 and DMS-0612878. VC acknowledges partial support from the NSF and the National Institutes of Health (NIH) through grants NSF-DMS-0314463 and NIH-5R01CA093650-03. QN acknowledges support from

the NSF and the NIH through grants NSF-DMS-0511169, NIH-R01GM75309 and NIH-R01GM67247.

REFERENCES

[1] J. Adam, *General aspects of modeling tumor growth and the immune response,in: A survey of models on tumor immune systems dynamics*, J. Adam and N. Bellomo eds, Birkhauser, Boston, (1996), 15-87.

[2] T. Alarcon, H.M. Byrne, and P.K. Maini, *A cellular automaton model for tumour growth in inhomogeneous environment*, J. Theor. Biol., **225** (2003), 257-274.

[3] A.R.A. Anderson, *A Hybrid Mathematical Model of Solid Tumour Invasion: The Importance of Cell Adhesion*, IMA Math. App. Med. Biol., **22** (2005), 163-186.

[4] A.R.A. Anderson and M.A.J. Chaplain, *Continuous and discrete mathematical models of tumor-induced angiogenesis*, Bull. Math. Biol., **60** (1998), 857-899.

[5] R.P. Araujo and D.L.S. McElwain, *A history of the study of solid tumour growth: The contribution of mathematical modelling*, Bull. Math. Biol., **66** (2004), 1039-1091.

[6] R.P. Araujo and D.L.S. McElwain, *A linear-elastic model of anisotropic tumor growth*, Euro. J. Appl. Math., **15** (2004), 365-384.

[7] R.P. Araujo and D.L.S. McElwain, *A mixture theory for the genesis of residual stress in growing tissues I: A general formulation*, SIAM J. Appl. Math., **65** (2005), 1261-1284.

[8] R.P. Araujo and D.L.S. McElwain, *A mixture theory for the genesis of residual stress in growing tissues II: Solutions to the biphasic equations for a multicell spheroid*, SIAM J. Appl. Math., **66** (2005), 447-467.

[9] C. Athale, Y. Mansury, and T.S. Deisboeck, *Simulating the impact of a molecular 'decision-process' on cellular phenotype and multicellular patterns in brain tumors*, J. Theor. Biol., **233** (2005), 469-481.

[10] K.E. Atkinson, The numerical solution of integral equations of the second kind, Cambridge University Press, 1997.

[11] N. Bellomo and L. Preziosi, *Modeling and mathematical problems related to tumor evolution and its interaction with the immune system*, Math. Comput. Model., **32** (2000), 413-452.

[12] H.M. Byrne, T. Alarcon, M.R. Owen, S.D. Webb, and P.K. Maini, *Modeling aspects of cancer dynamics: A review*, Phil. Trans. R. Soc. A, **364** (2006), 1563-1578.

[13] H.M. Byrne and M.A.J. Chaplain, *Growth of Nonnecrotic Tumors in the Presence and Absence of Inhibitors*, Math. Biosci., **130** (1995), 151-181.

[14] H.M. Byrne and M.A.J. Chaplain, *Growth of necrotic tumors in the presence and absence of inhibitors*, Math. Biosci., **135** (1996), 187-216.

[15] H.M. Byrne and M.A.J. Chaplain, *Modelling the role of cell-cell adhesion in the growth and development of carcinomas*, Math. Comput. Model., **24** (1996), 1-17.

[16] H.M. Byrne and P. Matthews, *Asymmetric growth of models of avascular solid tumors: exploiting symmetries*, IMA J. Math. Appl. Med. Biol., **19** (2002), 1-29.

[17] H.M. Byrne and L. Preziosi, *Modeling solid tumor growth using the theory of mixtures*, Math. Med. Biol., **20** (2003), 341-366.

[18] M.A.J. Chaplain, L. Graziano, and L. Preziosi, *Mathematical modelling of the loss of tissue compression responsiveness and its role in solid tumour development*, Math. Med. Biol., **23** (2006), 192-229.

[19] C.Y. Chen, H.M. Byrne, and J.R. King, *The influence of growth-induced stress from the surrounding medium on the development of multicell spheroids*, J. Math. Biol., **43** (2001), 191-220.

[20] D. Colton and R. Kress, Integral Equation Methods in Scattering Theory, Wiley-Interscience Publication, 1983.

[21] V. Cristini, J. Blawzdziewicz, and M. Loewenberg, *An adaptive mesh algorithm for evolving surfaces: Simulations of drop breakup and coalescence*, J. Comput. Phys., **168** (2001), 445-463.

[22] V. Cristini, H.B. Frieboes, R. Gatenby, S. Caserta, M. Ferrari, and J. Sinek, *Morphologic Instability and Cancer Invasion*, Clin Cancer Res., **11** (2005), 6772-6779.

[23] V. Cristini, X. Li, J. Lowengrub, and S. Wise, *Solid tumor growth: Mixture models*, in preparation.

[24] V. Cristini and J. Lowengrub, *Three-dimensional crystal growth I: Linear analysis and self-similar evolution*, J. Crystal Growth, **240** (2002), 267-276.

[25] V. Cristini and J. Lowengrub, *Three-dimensional crystal growth II: Nonlinear simulation and control of the Mullins-Sekerka instability*, J. Crystal Growth, **266** (2004), 552-567.
[26] V. Cristini, J. Lowengrub, and Q. Nie, *Nonlinear simulation of tumor growth*, J. Math. Biol., **46** (2003), 191-224.
[27] S. Dormann and A. Deutsch, *Modeling of self-organized avascular tumor growth with a hybrid cellular automaton*, In Silico Biology, **2** (2002), 393-406.
[28] H. Frieboes, S. Wise, J. Lowengrub, and V. Cristini, *Three-dimensional simulation of the growth of a multispecies tumor via a diffuse interface approach*, Bull. Math. Biol., in review.
[29] H.B. Frieboes, X. Zheng, C.-H. Sun, B. Tromberg, R. Gatenby, and V. Cristini, *An Integrated Computational/Experimental Model of Tumor Invasion*, Cancer Res., **66** (2006), 1597-1604.
[30] A. Friedman and F. Reitich, *Analysis of a mathematical model for the growth of tumors*, J. Math. Biol., **38** (1999), 262-284.
[31] R.A. Gatenby, E.T. Gawlinski, A.F. Gmitro, B. Kaylor, and R.J. Gillies, *Acid-Mediated Tumor Invasion: a Multidisciplinary Study*, Cancer Res., **66** (2006), 5216-5223.
[32] H.P. Greenspan, *Models for the Growth of a Solid Tumor by diffusion*, Stud. Appl. Math., **51** (1972), 317-340.
[33] H.P. Greenspan, *On the growth and stability of cell cultures and solid tumors*, J. Theor. Biol., **56** (1976), 229-242.
[34] C.S. Hogea, B.T. Murray, and J.A. Sethian, *Simulating complex tumor dynamics from avascular to vascular growth using a general level-set method*, J. Math. Biol., **53** (2006), 86-134.
[35] J.D. Jackson, Classical electrodynamics, New York: Wiley, 1999.
[36] S. Jbabdi, E. Mandonnet, H. Duffau, L. Capelle, K.R. Swanson, M. Pelegrini-Issac, R. Guillevin, and H. Benali, *Simulation of anisotropic growth of low-grade gliomas using diffusion tensor imaging*, Magn. Res. Med., **54** (2005), 616-624.
[37] Y. Jiang, J. Pjesivac-Grbovic, C. Cantrell, and J.P. Freyer, *A multiscale model for avascular tumor growth*, Biophys. J., **89** (2005), 3884-3894.
[38] A.R. Kansal, S. Torquato, G.R. Harsh IV, E.A. Chiocca, and T.S. Deisboeck, *Simulated brain tumor growth dynamics using a three-dimensional cellular automaton*, J. Theor. Biol., **203** (2000), 367-382.
[39] E. Khain and L.M. Sander, *Dynamics and pattern formation in invasive tumor growth*, Phys. Rev. Lett., **96** (2006) 188103.
[40] X. Li, *Ph.D. Thesis*, University of California at Irvine.
[41] P. Macklin and J. Lowengrub, *Evolving interfaces via gradients of geometry-dependent interior Poisson problems: application to tumor growth*, J. Comput. Phys., **203** (2005), 191-220.
[42] P. Macklin and J. Lowengrub, *An improved geometry-aware curvature discretization for level-set methods: Application to tumor growth*, J. Comput. Phys., **215** (2006), 392-401.
[43] P. Macklin and J. Lowengrub, *Nonlinear simulation of the effect of the microenvironment on tumor growth*, accepted by J. Theor. Biol..
[44] D.G. Mallett and L.G. de Pillis, *A Cellular Automata Model of Tumor-immune System Interactions*, J. Theor. Biol., **239** (2006), 334-350.
[45] Y. Mansury, M. Kimura, J. Lobo, and T.S. Deisboeck, *Emerging Patterns in Tumor Systems: Simulating the Dynamics of Multicellular Clusters with an Agent-based Spatial Agglomeration Model*, J. Theor. Biol., **219** (2002), 343-370.
[46] W.W. Mullins and R.F. Sekerka, *Morphological stability of a particle growing by diffusion or heat flow*, J. Appl. Phys., **34** (1963), 323-329.
[47] V. Quaranta, A.M. Weaver, P.T. Cummings, and A.R.A. Anderson, *Mathematical Modeling of Cancer: The future of prognosis and treatment*, Clinica Chimica Acta, **357** (2005), 173-179.
[48] T. Roose, P.A. Netti, L.L. Munn, Y. Boucher, and R. Jain, *Solid stress generated by spheroid growth estimated using a linear poroelastic model*, Microvascular Res., **66** (2003), 204-212.
[49] Y. Saad and M.H. Schultz, *GMRES: A Generalized Minimal Residual Algorithm for Solving Nonsymmetric Linear Systems*, SIAM J. Sci. Stat. Comput., **7** (1986), 856-869.
[50] S. Sanga, J.P. Sinek, H.B. Frieboes, J.P. Fruehauf, and V. Cristini, *Mathematical modeling of cancer progression and response to chemotherapy*, Expert. Rev. Anticancer Ther., **6** (2006), 1361-1376.
[51] K.R. Swanson, C. Bridge, J.D. Murray, and E.C. Alvord jr., *Virtual and real brain tumors: Using mathematical modeling to quantify glioma growth and invasion*, J. Neuro. Sci., **216** (2003), 1-10.
[52] S. Turner and J.A. Sherratt, *Intercellular adhesion and cancer invasion: A discrete simulation using the extended Potts model*, J. Theor. Biol., **216** (2002), 85-100.

[53] J. Wermer, Potential Theory, New York: Springer-Verlag, 1980.
[54] X. Zheng, S.M. Wise, and V. Cristini, *Nonlinear Simulation of Tumor Necrosis, Neo-Vascularization and Tissue Invasion via an Adaptive Finite-Element/Level-Set Method*, Bull. Math. Biol., **67** (2005) 211-259.
[55] A.Z. Zinchenko, M.A. Rother, and R.H. Davis, *A novel boundary-integral algorithm for viscous interaction of deformable drops*, Phys. Fluids, **9** (1997), 1493-1511.

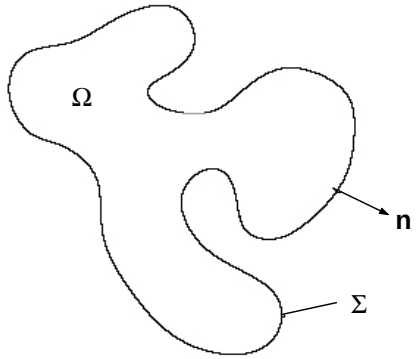

FIGURE 1. Diagram of a tumor. The tumor occupies the volume Ω, Σ is the interface between tumor tissue and health tissue, $\mathbf{n}$ is the unit outward normal to Σ.

Received December 15, 2006; revised January 2007.

E-mail address: xli@math.uci.edu; cristini@math.uci.edu
E-mail address: qnie@math.uci.edu; lowengrb@math.uci.edu

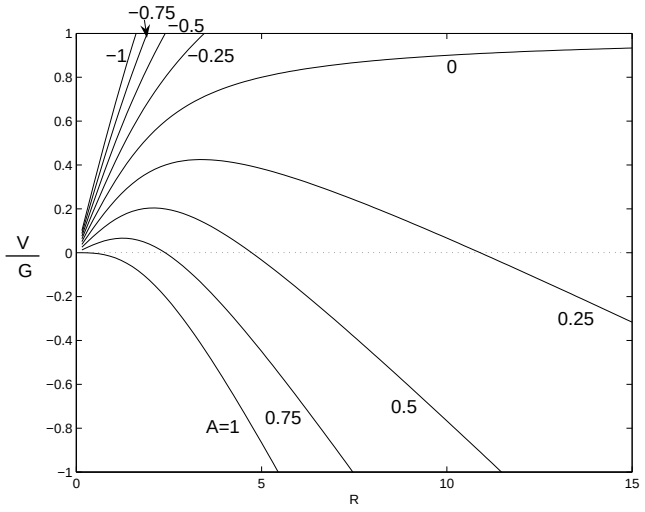

(a)

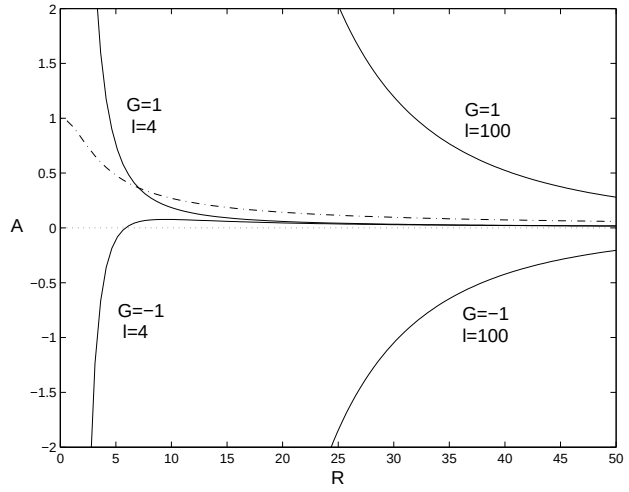

(b)

FIGURE 2. (a): Rescaled rate of growth V/G as a function of rescaled tumor radius R for radially symmetric tumor growth; A labelled. (b): Apoptosis parameter A_c as a function of unperturbed radius R from condition (20) (solid); G and l labelled. The dash-dotted curve corresponds to stationary radii.

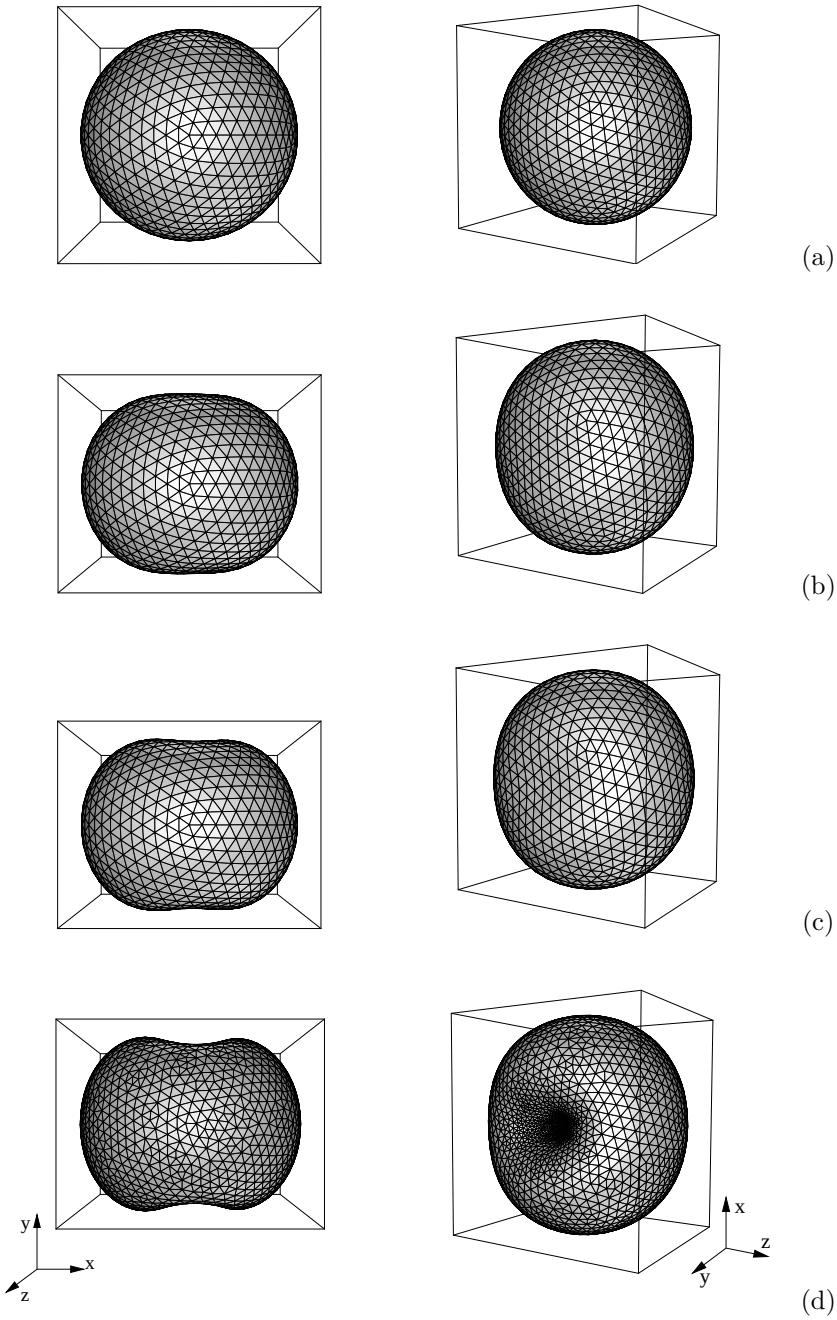

FIGURE 3. Evolution of the tumor surface in the low-vascularization regime, $A = 0.5$, $G = 20$, and initial tumor surface as in Eqn. (60). (a) $t = 0$, $\bar{\delta} = 0.0137$, $\mathcal{S} = 3.0$ (b) $t = 2.21$, $\bar{\delta} = 0.12$, $\mathcal{S} = 4.732$ (c) $t = 2.42$, $\bar{\delta} = 0.2$, $\mathcal{S} = 4.745$ (d) $t = 2.668$, $\bar{\delta} = 0.496$, $\mathcal{S} = 4.781$

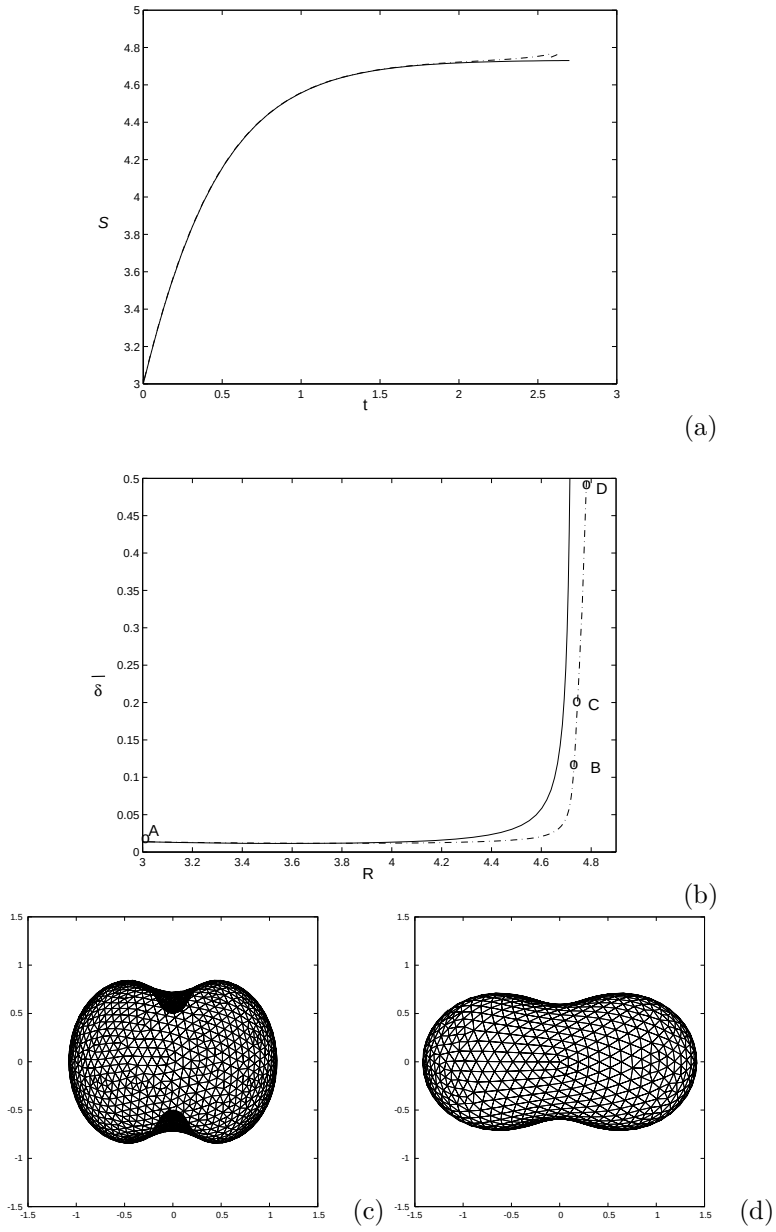

FIGURE 4. Comparison of linear analysis (Solid) and nonlinear results (Dash-dotted) for the simulation in Fig. 3. (a). The scale factor $\mathcal{S}(t)$; (b). The perturbation size $\bar{\delta}$; The circles correspond to the morphologies shown in Fig. 3(a)-(d). (c). Nonlinear tumor morphology at $t = 2.668$, with $\mathcal{S} = 4.78$ and $\bar{\delta} = 0.496$; (d). Linear solution morphology (shown with a triangulated mesh) at the same time, $\mathcal{S} = 4.73$ and $\bar{\delta} = 0.42$. View from the positive z-axis.

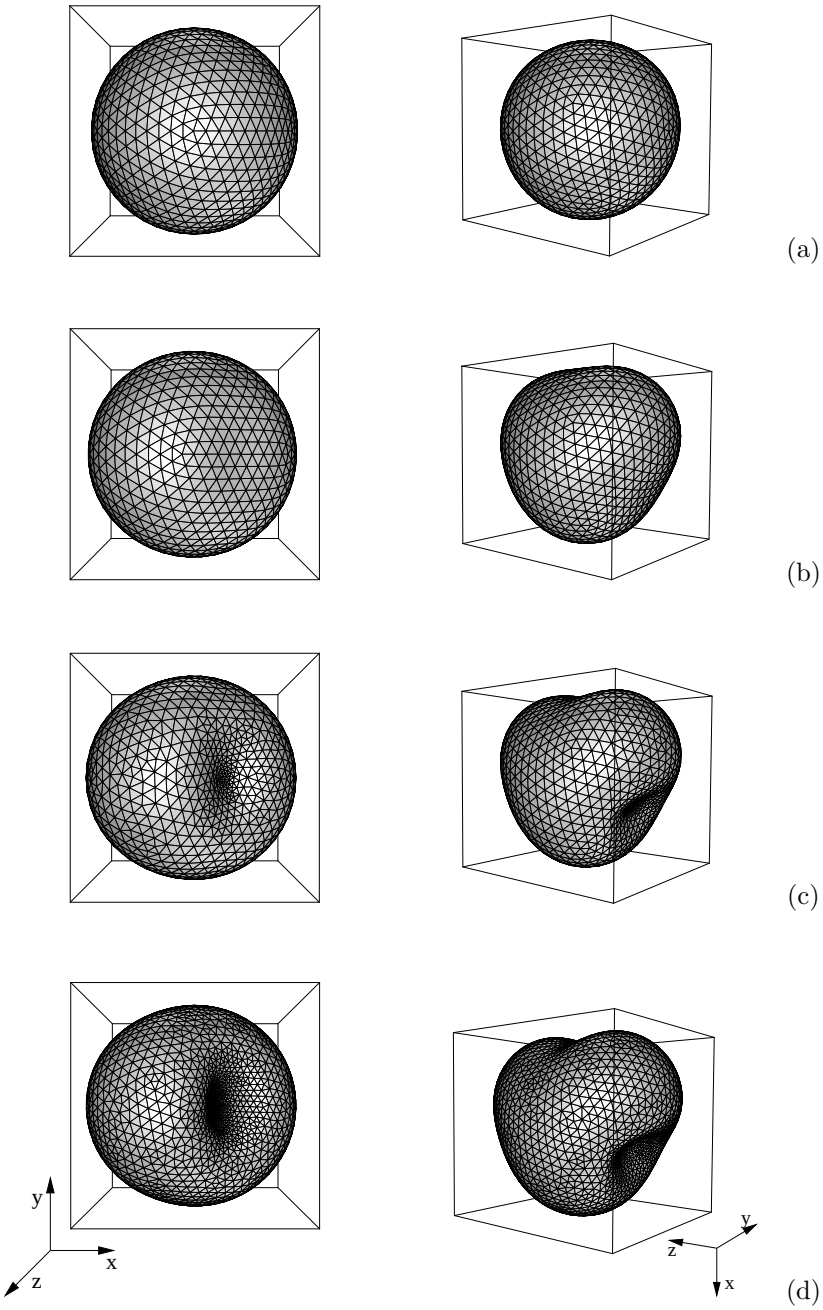

FIGURE 5. Evolution of the tumor surface in the low-vascularization regime, $A = 0.5$, $G = 20$, and initial tumor surface as in Eqn. (62). (a) $t = 0$, $\bar{\delta} = 0.0158$, $\mathcal{S} = 3.0$ (b) $t = 1.8$, $\bar{\delta} = 0.123$, $\mathcal{S} = 4.722$ (c) $t = 2.04$, $\bar{\delta} = 0.3$, $\mathcal{S} = 4.76$ (d) $t = 2.145$, $\bar{\delta} = 0.476$, $\mathcal{S} = 4.805$

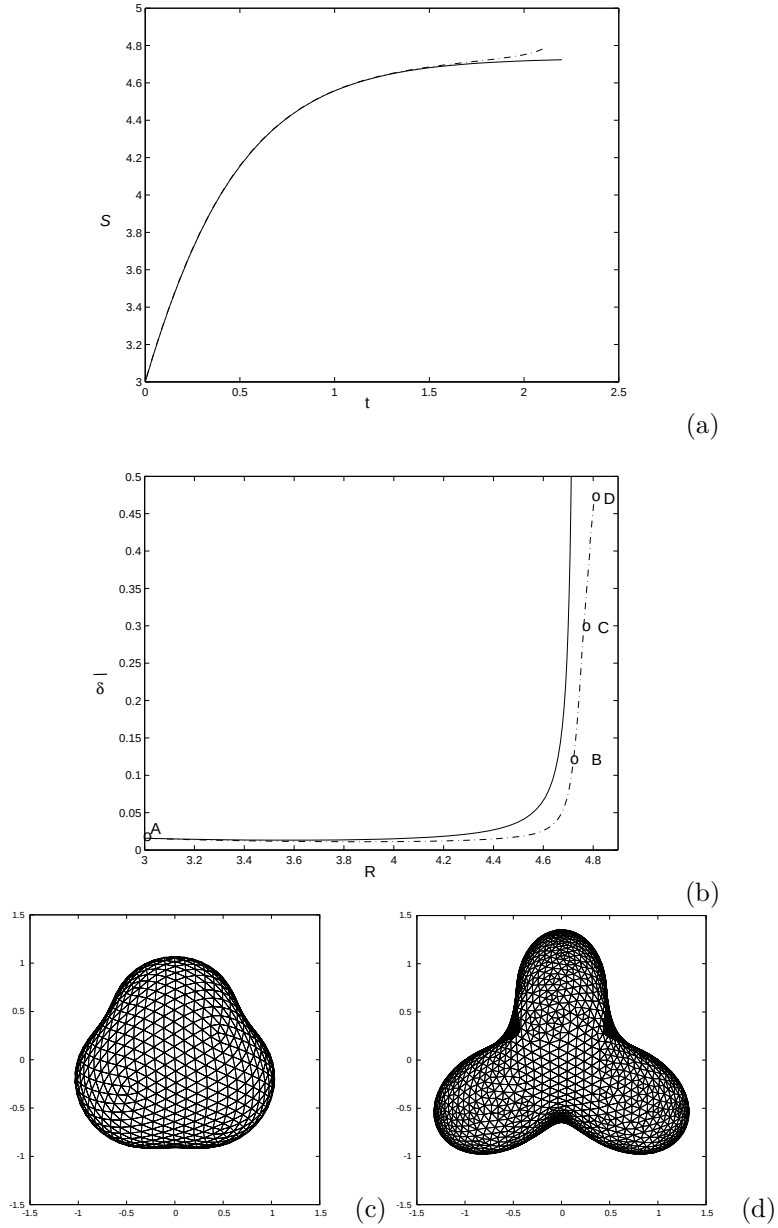

FIGURE 6. Comparison of linear analysis (Solid) and nonlinear results (Dash-dotted) for the simulation in Fig. 5. (a). The scale factor $\mathcal{S}(t)$; (b). The perturbation size $\bar{\delta}$; The circles correspond to the morphologies shown in Fig. 5(a)-(d). (c). Nonlinear tumor morphology at $t = 1.88$, with $\mathcal{S} = 4.732$ and $\bar{\delta} = 0.156$; (d). Linear solution morphology (shown with a triangulated mesh) at the same time, $\mathcal{S} = 4.712$ and $\bar{\delta} = 0.476$. View from the positive y-axis.

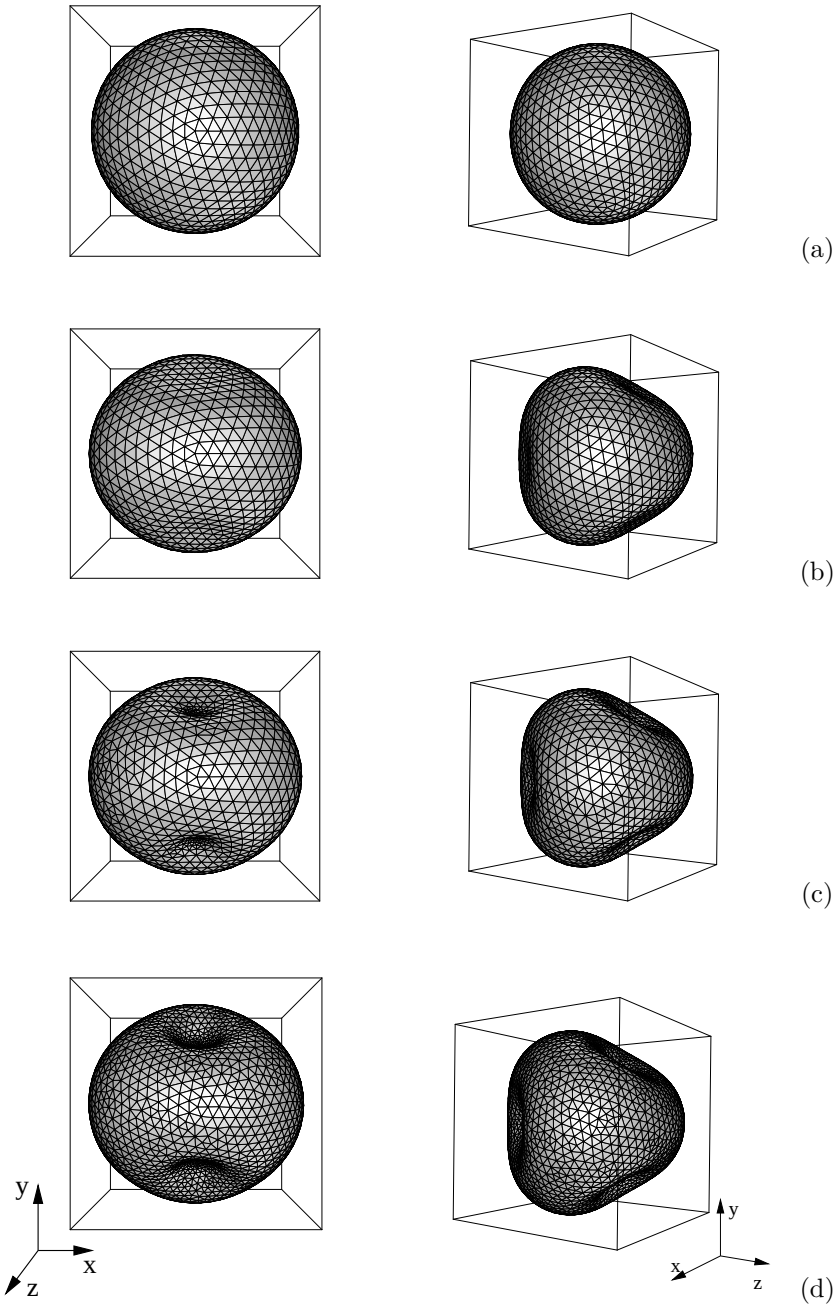

FIGURE 7. Evolution of the tumor surface in the low-vascularization regime, $A = 0.5$, $G = 20$, and initial tumor surface as in Eqn. (63). (a) $t = 0$, $\bar{\delta} = 0.014$, $\mathcal{S} = 3.0$ (b) $t = 1.88$, $\bar{\delta} = 0.152$, $\mathcal{S} = 4.734$ (c) $t = 2.02$, $\bar{\delta} = 0.254$, $\mathcal{S} = 4.761$ (d) $t = 2.107$, $\bar{\delta} = 0.376$, $\mathcal{S} = 4.798$

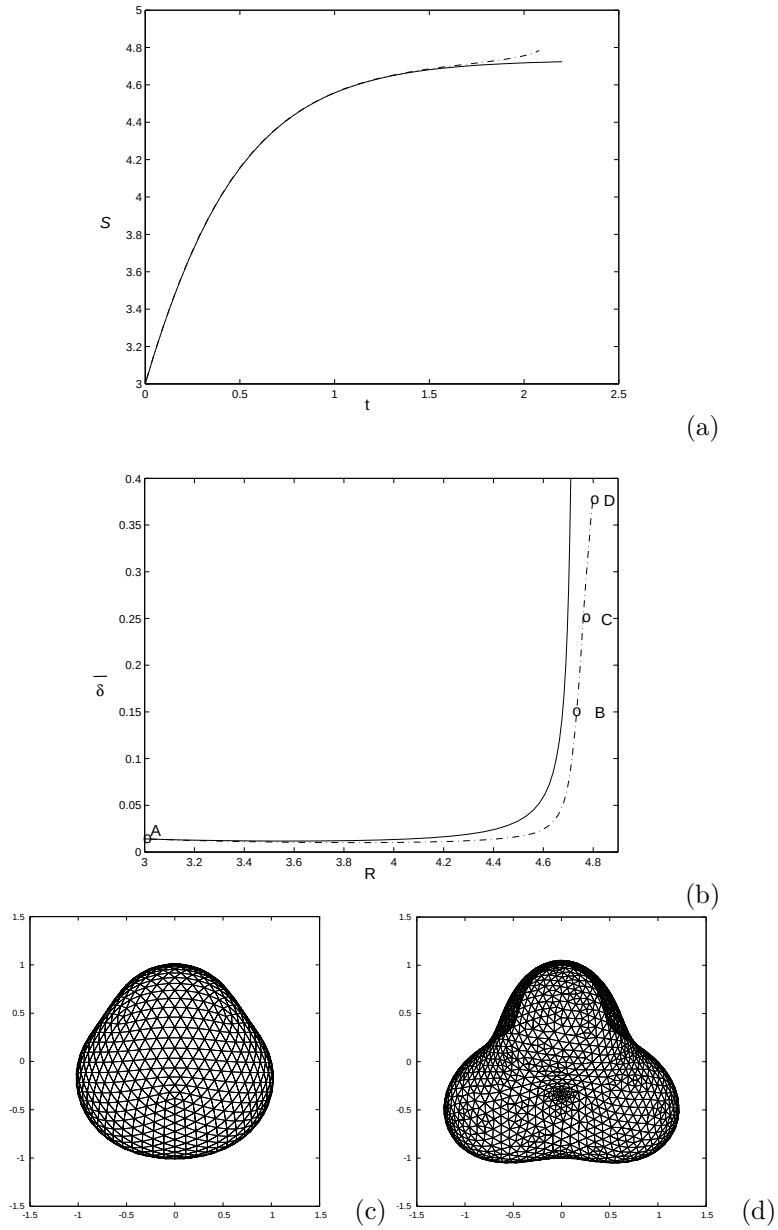

FIGURE 8. Comparison of linear analysis (Solid) and nonlinear results (Dash-dotted) for the simulation in Fig. 7. (a). The scale factor $\mathcal{S}(t)$; (b). The perturbation size $\bar{\delta}$; The circles correspond to the morphologies shown in Fig. 7(a)-(d). (c). Nonlinear tumor morphology at $t = 1.84$, with $\mathcal{S} = 4.728$ and $\bar{\delta} = 0.134$; (d). Linear solution morphology (shown with a triangulated mesh) at the same time, $\mathcal{S} = 4.710$ and $\bar{\delta} = 0.376$. View from the positive x-axis.